Report

Cell Reports

Inhibitory projections connecting the dentate gyri in the two hemispheres support spatial and contextual memory

Graphical abstract

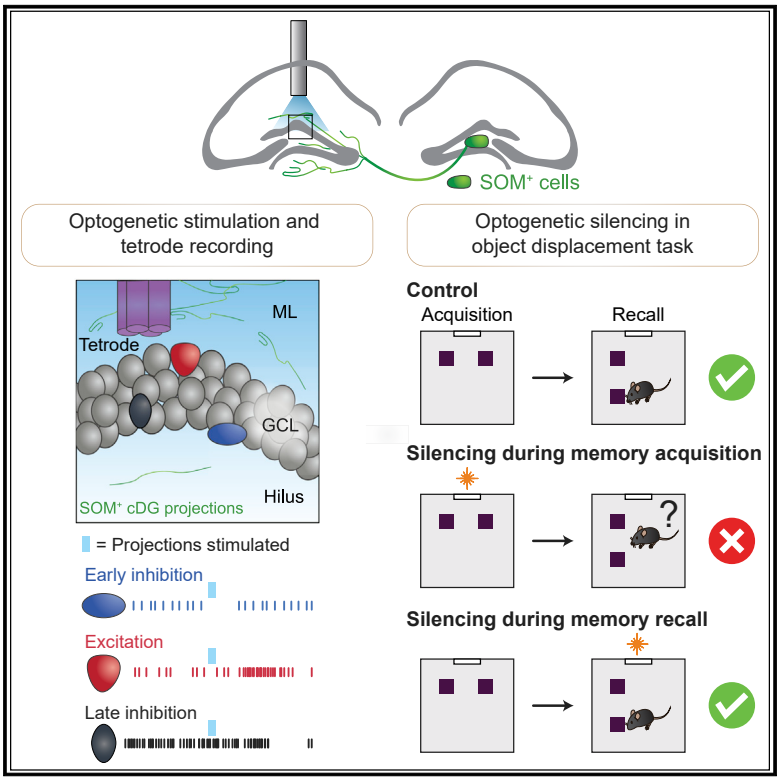

Highlights

- SOM$^+$ cDG projections control DG activity in a cell-type-specific manner
- Activation of SOM$^+$ cDG projections is required for memory formation
- Activation of SOM$^+$ cDG projections is sufficient to disrupt memory recall

Authors

Ting-Yun Yen, Xu Huang, Duncan Archibald Allan MacLaren, Magdalene Isabell Schlesiger, Hannah Monyer, Cheng-Chang Lien

Correspondence

h.monyer@dkfz-heidelberg.de (H.M.), cclien@ym.edu.tw (C.-C.L.)

In brief

Yen et al. show that a subset of SOM$^+$ GABAergic cells mediates long-range, inter-DG inhibition by targeting specific types of DG neurons. Although the projections are sparse, they regulate DG activity in freely moving mice, thereby supporting spatial and contextual memory formation.

Yen et al., 2022, Cell Reports *39*, 110831
May 17, 2022
https://doi.org/10.1016/j.celrep.2022.110831

CellPress

Cell Reports

CellPress
OPEN ACCESS

Report

Inhibitory projections connecting the dentate gyri in the two hemispheres support spatial and contextual memory

Ting-Yun Yen,[1,2,3] Xu Huang,[3] Duncan Archibald Allan MacLaren,[3] Magdalene Isabell Schlesiger,[3] Hannah Monyer,[3,4,*] and Cheng-Chang Lien[1,2,*]

[1]Taiwan International Graduate Program in Molecular Medicine, National Yang Ming Chiao Tung University and Academia Sinica, Taipei, Taiwan

[2]Institute of Neuroscience, National Yang Ming Chiao Tung University, Taipei 112, Taiwan

[3]Department of Clinical Neurobiology at the Medical Faculty of Heidelberg University and German Cancer Research Center (DKFZ), Im Neuenheimer Feld 280, 69120 Heidelberg, Germany

[4]Lead contact

*Correspondence: h.monyer@dkfz-heidelberg.de (H.M.), cclien@ym.edu.tw (C.-C.L.)

https://doi.org/10.1016/j.celrep.2022.110831

SUMMARY

The dentate gyrus (DG) receives substantial input from the homologous brain area of the contralateral hemisphere. This input is by and large excitatory. Viral-tracing experiments provided anatomical evidence for the existence of GABAergic connectivity between the two DGs, but the function of these projections has remained elusive. Combining electrophysiological and optogenetic approaches, we demonstrate that somatostatin-expressing contralateral DG (SOM^+ cDG)-projecting neurons preferentially engage dendrite-targeting interneurons over principal neurons. Single-unit recordings from freely moving mice reveal that optogenetic stimulation of SOM^+ cDG projections modulates the activity of GABAergic neurons and principal neurons over multiple timescales. Importantly, we demonstrate that optogenetic silencing of SOM^+ cDG projections during spatial memory encoding, but not during memory retrieval, results in compromised DG-dependent memory. Moreover, optogenetic stimulation of SOM^+ cDG projections is sufficient to disrupt contextual memory recall. Collectively, our findings reveal that SOM^+ long-range projections mediate inter-DG inhibition and contribute to learning and memory.

INTRODUCTION

The hippocampus is a key brain area involved in processing episodic memory (Olton et al., 1979; Tulving and Markowitsch, 1998). Cortical inputs reach the hippocampus via the canonical trisynaptic pathway, engaging the dentate gyrus (DG) as the first relay station for information processing (Amaral et al., 2007; Jonas and Lisman, 2014; McNaughton and Barnes, 1977; van Strien et al., 2009). Sparse activation of DG granule cells (GCs), which is thought to subserve pattern separation, transforms cortical information into distinct output patterns that are transmitted to the downstream CA3 area (Leutgeb et al., 2007; McNaughton and Morris, 1987; Neunuebel and Knierim, 2014; Yassa and Stark, 2011). The sparse activation of GCs is to a large extent under the control of local-circuit interneurons (Halasy and Somogyi, 1993; Sik et al., 1997; Sloviter and Brisman, 1995) that contribute to the high activation threshold of GCs, thus increasing the signal-to-noise ratio upon cortical activation (Espinoza et al., 2018; Lee et al., 2016). Therefore, loss of inhibition or inadequate inhibition leads to impaired performance in several hippocampus-dependent memory tasks (Deng et al., 2019; Donato et al., 2013; Morales et al., 2021; Murray et al., 2011; Stefanelli et al., 2016; Xia et al., 2017).

GABAergic cells are crucial in maintaining the excitation-inhibition balance of neural circuits (Anderson et al., 2000; Bhatia et al., 2019; Okun and Lampl, 2008) and contribute to the modulation of network oscillations in several brain areas (Atallah and Scanziani, 2009; Bartos et al., 2007). Local interneurons are not the only source of inhibition in cortical networks. Thus, there is increasing evidence that GABAergic projection neurons modulate the activity of remotely located cortical brain areas (Basu et al., 2016; Caputi et al., 2013; Eyre and Bartos, 2019; Jinno et al., 2007; Melzer et al., 2012; Melzer and Monyer, 2020). GABAergic projection neurons exert their influence in either heterologous or homologous brain regions. For instance, the medial entorhinal cortex-hippocampus projections (Melzer et al., 2012) connect functionally distinct brain areas within one hemisphere, whereas the DG-DG projections that we focus on here (Eyre and Bartos, 2019) ensure interhemispheric connectivity between homologous brain areas.

Connectivity between homologous brain areas has been demonstrated at the anatomical and electrophysiological level for many hippocampal subfields, including the DG. Most projections providing the direct interhemispheric interaction between functionally similar hippocampal areas are excitatory in nature. For instance, hilar mossy cells (MCs) provide bilateral

connectivity between the left and the right DG (Deadwyler et al., 1975). Interestingly, as MCs preferentially innervate interneurons, the net effect on GCs is primarily inhibitory (Buzsáki and Czéh, 1981; Buzsáki and Eidelberg, 1981; Bilkey and Goddard, 1987; Wang et al., 2021). Here we studied GABAergic projection neurons that connect the two DG in the right and left hemispheres. Their existence was first inferred based on retrograde tracing experiments (Ribak et al., 1986) and corroborated much later by employing an anterograde viral-tracing approach (Melzer et al., 2012). A more detailed anatomical characterization of these somatostatin-expressing (SOM^+) cells ensued (Eyre and Bartos, 2019), but the identity of the target cells in the contralateral hemisphere and their functional role *in vivo* have remained unknown.

In this study, we investigate the synaptic transmission of the contralateral DG (cDG) projections and their role in DG-dependent behavioral tests using a combination of optogenetic and *ex vivo* and *in vivo* electrophysiological approaches that allow the selective manipulation of cDG projection terminals. We demonstrate that connections formed by GABAergic projection neurons, although weak and sparse, are sufficient to modulate neuronal activity in the cDG and contribute to memory formation and retrieval.

RESULTS

GABAergic SOM^+ cDG projections differentially innervate DG neurons

To establish the identity of GABAergic source cells that project to the cDG, we performed viral-tracing experiments. An adeno-associated virus (AAV) allowing the Cre-dependent transduction of ChR2-mCherry was injected unilaterally into the dorsal DG of genetically modified mice, expressing Cre recombinase in distinct GABAergic neurons (Figures 1A, 1B, and S1A–S1D). Three weeks and more following the viral injection, mCherry-labeled axons were visualized in the cDG of GAD2- and SOM-Cre mice, and also, but to a lesser extent, in VIP- and PV-Cre mice (Figures 1C and S1B–S1E). There was no labeling of neurons in the contralateral hemisphere, excluding both transsynaptic spread or retrograde transport of viral particles (Figure S2A).

Given that the SOM^+ projections were denser than the other 2 GABAergic cell subtypes, we analyzed these projections in more detail. Previous immunohistochemical studies demonstrated that in the dorsal DG, SOM^+ cells localized to the hilus (Figure S2B; Amaral et al., 1988; Bakst et al., 1986; Morrison et al., 1982). Indeed, in agreement with this and also with a recent study (Eyre and Bartos, 2019), at the injection site, mCherry-labeled neurons were located in the hilus (Figures 1B and S2A), and axon terminals were observed mostly in the hilus and the outer molecular layer (OML), with a clear preference for the latter. In the contralateral hemisphere, mCherry-labeled axons were found in the homologous areas (Figures 1C and S2C), namely the hilus (Figure 1C, boxed region 2) and the OML (Figure 1C, boxed regions 1 and 3). To further support our findings, we injected the retrograde tracer CTB-555 into one DG (Figure S1F). Upon inspection of the contralateral hippocampus 5 days post injection, we detected CTB^+ cells in the hilus (Figure S1G, top) but not in the CA1 and CA3 (Figure S1G, bottom). The retrogradely labeled CTB^+ neurons in the hilus significantly outnumbered the anterogradely labeled $mCherry^+$ neurons (Figures 1B and S1G; CTB^+ cells, ~45 cells/slice, 8 slices from 2 mice; $mCherry^+$ cells, ~6 cells/slice, 16 slices from 4 mice), which is not surprising, as MCs are known to project to the cDG. In agreement with the notion that MCs selectively express GluR2/3 but not SOM (Fujise and Kosaka, 1999; Lein et al., 2007; Wang et al., 2021), CTB positivity was detected in GluR2/3 (i.e., MCs) (Figure S1H) and SOM^+ cells (Figures S1I and S1J).

To investigate the connectivity pattern of SOM^+ cells in the cDG, a ChR2-eYFP-expressing virus was injected into one DG, and whole-cell patch-clamp recordings were performed from various types of neurons in the cDG (Figure 1D). Using a high Cl^- internal solution, brief photostimulation of ChR2-expressing axons evoked inward currents within 5 ms in GCs and morphologically defined interneurons of the cDG. The responses were comparable to the baseline condition after applying kynurenic acid (2 mM), but were completely blocked by the $GABA_A$ receptor antagonist gabazine (1 μM) (Figures 1E and S3A–S3C), providing evidence for the inhibitory nature of the optogenetically activated synaptic terminals. Light-evoked responses were detected also in MCs and in various types of dendrite-targeting interneurons (D-INs) but not in basket cells (BC) (Figures 1F, left, and S3D–S3I; Table S1). Further analysis of the light-evoked responses revealed that, despite the large variation in individual cell types, the inhibitory postsynaptic conductance (IPSG) of most D-INs was greater than that of GCs (Figure 1F, right). To control for conductance differences in cells recorded from different slices, we analyzed evoked responses from recorded D-INs and GCs in the same slice. Indeed, in most instances (20 of 23), the IPSG of the current induced in the D-IN was greater than that of the simultaneously recorded GC (Figure 1G).

Stimulating SOM^+ cDG projections modulates DG activity in freely moving mice

To test the effect of SOM^+ cDG projection activation in freely moving mice, we injected a ChR2-mCherry virus into the hilar region of one DG of SOM-Cre mice, and stimulated axon terminals in the cDG. Tetrodes and an optic fiber were implanted above the cDG (Figures 2A, top, and S4A) and the tetrodes were advanced gradually after each recording. Single-unit activity was recorded while the mice were foraging in an open-field environment containing two scented objects (Figures 2A, bottom, and S4B). Such an enrichment of the environment was previously reported to increase the activity of DG neurons known to exhibit normally sparse firing (Heale and Vanderwolf, 1994; Huckleberry et al., 2015; Kirschen et al., 2017). The mice do not have a preference for the scented objects during the recording sessions (Figures S4C–S4E). Of the recorded DG neurons (n = 1,052 neurons) only a subset (n = 61 neurons) responded to the 10 Hz photostimulation. We utilized peristimulus time histograms (Figure 2B) to further categorize responsive neurons considering the change in firing rate and the response latency. Three groups were identified. Specifically, we distinguished neurons that were inhibited early (I_E; n = 7 neurons, latency 3.5–6.5 ms) or late (I_L; n = 44 neurons, latency 10.5–28.5 ms) and neurons that were excited (E; n = 10 neurons, latency 4.5–17.5 ms) following

CellPress
OPEN ACCESS

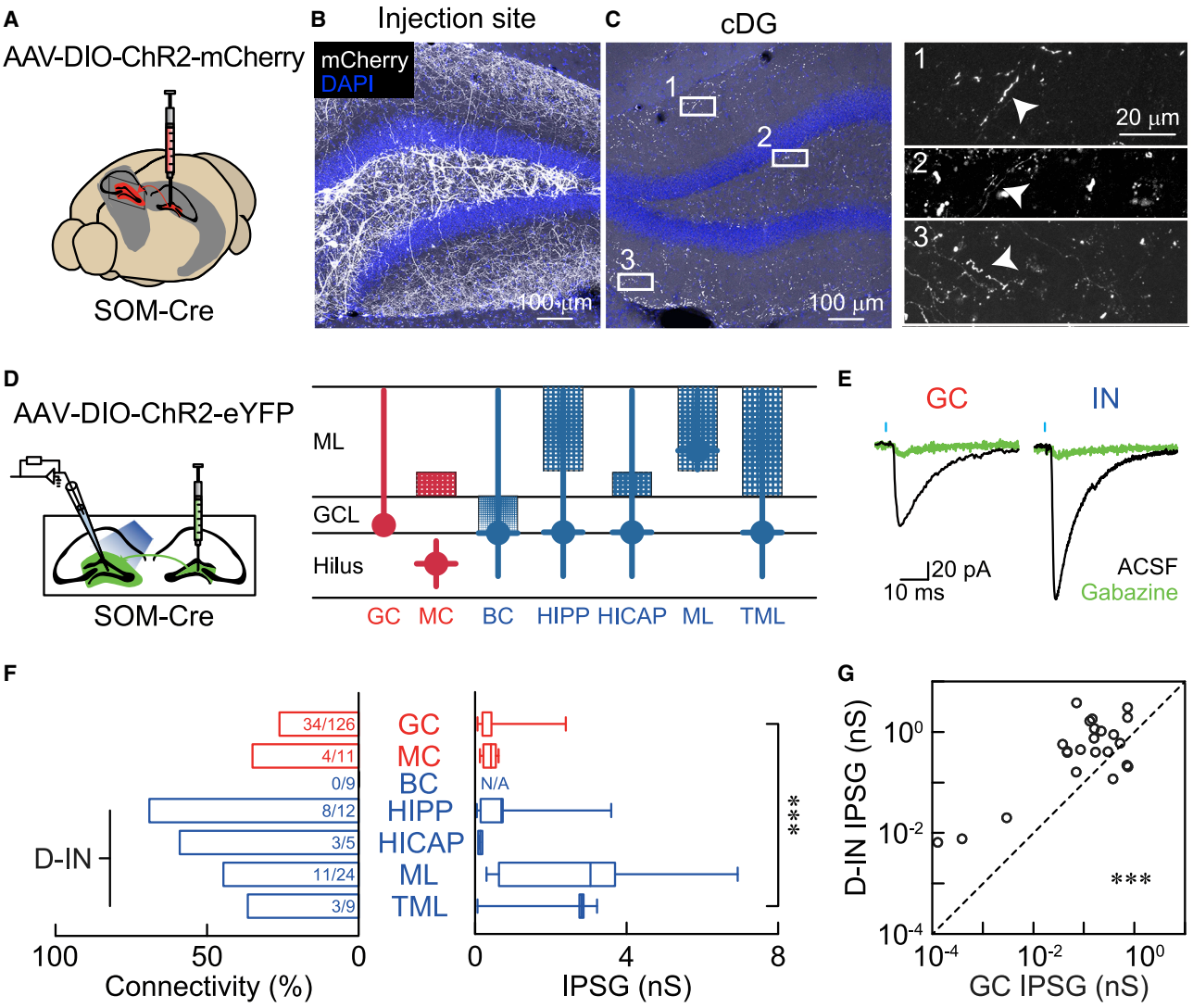

Figure 1. GABAergic SOM⁺ cDG projections differentially innervate DG neurons

(A) Schematic of viral injection into a SOM-Cre mouse.

(B) Expression of ChR2-mCherry and 4′,6-diamidino-2-phenylindole (DAPI) at the virus injection site. Somata labeled by mCherry are detectable in the hilus and axons in the OML and the hilus.

(C) Expression of mCherry and DAPI in the cDG. Right, enlarged views of the indicated areas in the left image. Arrowheads indicate mCherry-labeled axons.

(D) Left, experimental schematic. Right, summary diagram of two principal neurons (red) and five morphophysiologically distinct interneuron subtypes (blue). Filled circles mark the location of the cell body; the thick lines indicate the dendritic trees; the hatched boxes are the domains where the axons of the indicated interneuron types arborize primarily. GC, granule cell; MC, mossy cell; BC, basket cell; HICAP, hilar commissural-associational pathway-related cell; HIPP, hilar perforant path-associated cell; ML, molecular layer cell; TML, total molecular layer cell.

(E) Whole-cell patch-clamp recordings from a GC and an interneuron (IN) and 470 nm LED illumination of nearby cDG projections. Representative traces showing gabazine (1 µM)-induced blockage of postsynaptic currents evoked by photostimulation of cDG projections (see also Figure S3).

(F) Left, quantitative evaluation of the connectivity between cDG projections and various types of target cells in the cDG (see also Figure S2). Dendrite-targeting interneurons are marked as D-INs. Right, corresponding inhibitory postsynaptic conductances (IPSGs) from each cell type. ***p = 0.0004, Kruskal-Wallis test. Box-and-whisker plots indicate the median, interquartile range, and minimum to maximum values.

(G) IPSGs from simultaneously recorded D-INs and GCs. ***p < 0.001, Mann-Whitney U test (N_{pairs} = 23, U = 132).

photostimulation (Figure S4F). Based on the distribution of response latencies, the cutoff value between I_E and I_L cells was set to 7 ms.

We wondered how the three groups of neurons correlate with previously established criteria for functionally distinct DG neuronal subtypes (Senzai and Buzsáki, 2017). Thus, according to these authors, trough-to-peak latency of the spike waveform and burst index are key parameters for the separation of DG neurons into excitatory neurons (quadrant I), inhibitory neurons with a narrow spike waveform (quadrants II and III), and inhibitory

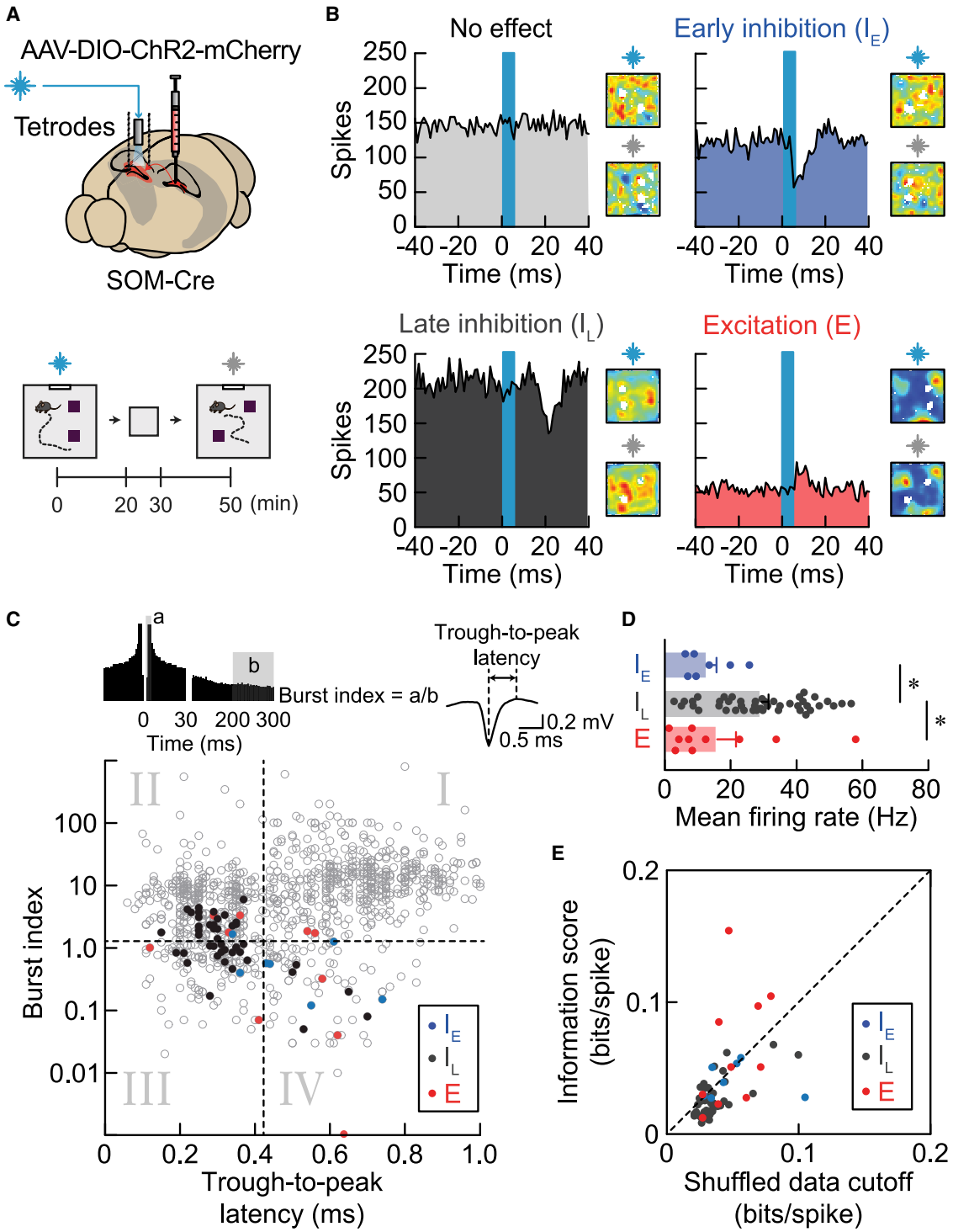

Figure 2. Stimulating SOM$^+$ cDG projections modulates DG activity in freely moving mice

(A) Top, schematic of the viral injection, and implantation of tetrodes and an optic fiber in the cDG (n = 13 mice). Bottom, recording paradigm. Blue laser stimulation at 10 Hz with a 5 ms duration is delivered in one of the two exploration sessions. The order of blue light delivery in the two sessions alternates from one day to the other. The objects are placed into the exploration chamber to increase the activity of DG neurons.

(B) Peristimulus time histograms of neuronal firing in response to photostimulation. The four illustrated neurons show either no effect (1,052 neurons), early inhibition (I_E; 7 neurons), late inhibition (I_L; 44 neurons), or excitation (E; 10 neurons). Spatial firing rate maps in light-on (top) and light-off (bottom) sessions are shown next to each histogram. The heatmaps are colored such that red indicates maximal firing rate and blue indicates no firing.

(legend continued on next page)

neurons with a wide spike waveform (quadrant IV). Indeed, neurons in quadrant I characterized by a lower mean firing rate and a higher information score were putative excitatory cells, while neurons in quadrants II, III, and IV, with a higher mean firing rate and a lower information score, were putative interneurons (Figures S4G and S4H). Most I_E and I_L neurons mapped onto quadrants IV and II/III, thus corresponding to wide- and narrow-waveform interneurons, respectively, while E neurons could be any cell type (Figure 2C). Narrow-waveform inhibitory neurons exhibit higher firing rates than wide-waveform inhibitory neurons (Morales et al., 2021; Senzai and Buzsáki, 2017). Indeed, I_L neurons exhibited significantly higher mean firing rates during light-off sessions than I_E or E neurons (Figure 2D). The firing-rate maps of both I_E and I_L neurons showed little spatial selectivity, whereas some E neurons exhibited spatial firing specificity (Figure 2B). Some GCs and MCs were shown to exhibit spatial selectivity (GoodSmith et al., 2017, 2019). Accordingly, we found four E cells with higher information scores than what was expected by chance (Figure 2E). The information score of the spatially tuned E cells, however, was lower than that typically reported for GCs and MCs (Gil et al., 2018; GoodSmith et al., 2017, 2019), and may depend on the exact recording conditions. Of all neurons responding to laser stimulation, the majority was categorized as I_L (44 of 61 responsive cells, 72%). Since I_L neurons were characterized by high mean firing rates and narrow spike waveforms, they are very likely fast-spiking inhibitory neurons.

Considering the chosen cutoff value of 7 ms ($> I_E$ and $< I_L$), it is safe to assume that the modulatory photostimulation-induced effect on most E cells and I_L cells is polysynaptic. To better understand the sequence of events, we performed again *in vitro* recordings in acute slices. We recorded in current clamp mode and low chloride concentration from GCs and molecular-layer interneurons, and found that upon pharmacological silencing of the projections (CNO wash-in), the latter increased, whereas the former decreased, their firing (Figure S4I). This is consistent with the *in vivo* results, where we obtained the opposite when activating the projections.

Stimulating SOM$^+$ cDG projections disrupts contextual memory

We next tested whether the artificial activation of SOM$^+$ ChR2-expressing axons in the cDG at the same frequency as used in our *in vivo* recordings was sufficient to disrupt memory in a context-reward memory task. SOM-Cre mice were injected with a DIO-ChR2-mCherry AAV or a control AAV (DIO-eYFP only) into one DG, and an optical fiber was implanted above the cDG. The mice were subsequently subjected to a conditioned place preference (CPP) task where one context was repeatedly associated with a reward (ethanol) and another context with a neutral stimulus (saline) (Figures 3A and 3B; see also STAR Methods). Mice received 10 Hz, 473 nm photostimulation on the test day when they had free access to both contexts. The control mice that received photostimulation during the test session showed a significant preference for the reward-paired context (increased CPP scores) (Figure 3C) and traveled farther in the reward context compared with the control context (Figure 3D). In contrast, ChR2 mice that received 10 Hz photostimulation during the test session neither exhibited a preference for the reward context (Figure 3C) nor traveled farther in this context (Figure 3D).

Silencing SOM$^+$ cDG projections during memory acquisition, but not retrieval, impairs spatial memory

Finally, since there is good evidence that the hippocampus processes spatial and non-spatial information (Lenck-Santini et al., 2005; O'Keefe, 1999; Wiener et al., 1989), we examined the effect of silencing SOM$^+$ cDG projections on behavioral tasks that require spatial and object memory (Ennaceur and Delacour, 1988). SOM-Cre mice were injected with a DIO-NpHR-eYFP AAV or a control AAV (DIO-eYFP) into the hilar region of one DG and implanted with an optical fiber above the cDG. The mice were subsequently tested in an object displacement (OD) and object recognition (OR) memory task (Figure 4A). Continuous photoinhibition was delivered during either the sample or the test phase in each task (Figures 4B and 4E). Spatial and object memory were evaluated during the test trial by calculating the discrimination index (DI) from the exploration time for the displaced object (OD) or novel object (OR) and that for the familiar location (in OD) or familiar object (in OR) (see also STAR Methods). In OD, both the control mice and the NpHR mice showed a preference for the object in a novel location when sham laser inhibition was delivered either during the sample sessions or during the test sessions (Figures 4C and 4D). In contrast, silencing the SOM$^+$ cDG projections during the OD sample trial blocked the preference for the displaced object during the subsequent test trial in the NpHR mice but not in the control mice (Figure 4C). Silencing the SOM$^+$ cDG projections during the test trials in the OD task did not affect the preference for the object in a novel location (Figure 4D). Next, we examined the effect of silencing the SOM$^+$ cDG projections in the OR task (Figure 4E). Silencing the SOM$^+$ cDG projections in either the sample or the test session had no effect on the preference for the novel object during the test session (Figures 4F and 4G). There was no difference in distance traveled in the laser-on condition between control and NpHR mice, neither in the OD nor in the OR task (Figure S5). Also, there was no preference for one of the two objects, neither in control nor in NpHR mice during the sample session (data not shown).

DISCUSSION

Here we combined viral-tracing, connectivity studies in acute slices; *in vivo* electrophysiology; and behavioral experiments to study GABAergic projections that connect the DGs in the

(C) Trough-to-peak latency and burst index of all recorded DG cells (open circles) and of the neurons that respond to photostimulation with I_E (blue), I_L (black), or E (red). The vertical dashed line is the cutoff value to isolate narrow-waveform inhibitory neurons (trough-to-peak latency <0.425 ms). The horizontal dashed line at burst index 1.2 is used to distinguish excitatory cells from wide-waveform inhibitory neurons.
(D) Mean firing rates of the responsive cells during light-off sessions. Bar graphs represent the mean + SEM. *$p < 0.05$, Kruskal-Wallis test.
(E) Information scores of the responsive cells during light-off sessions compared with the 95th percentile of information scores obtained from shuffled data.

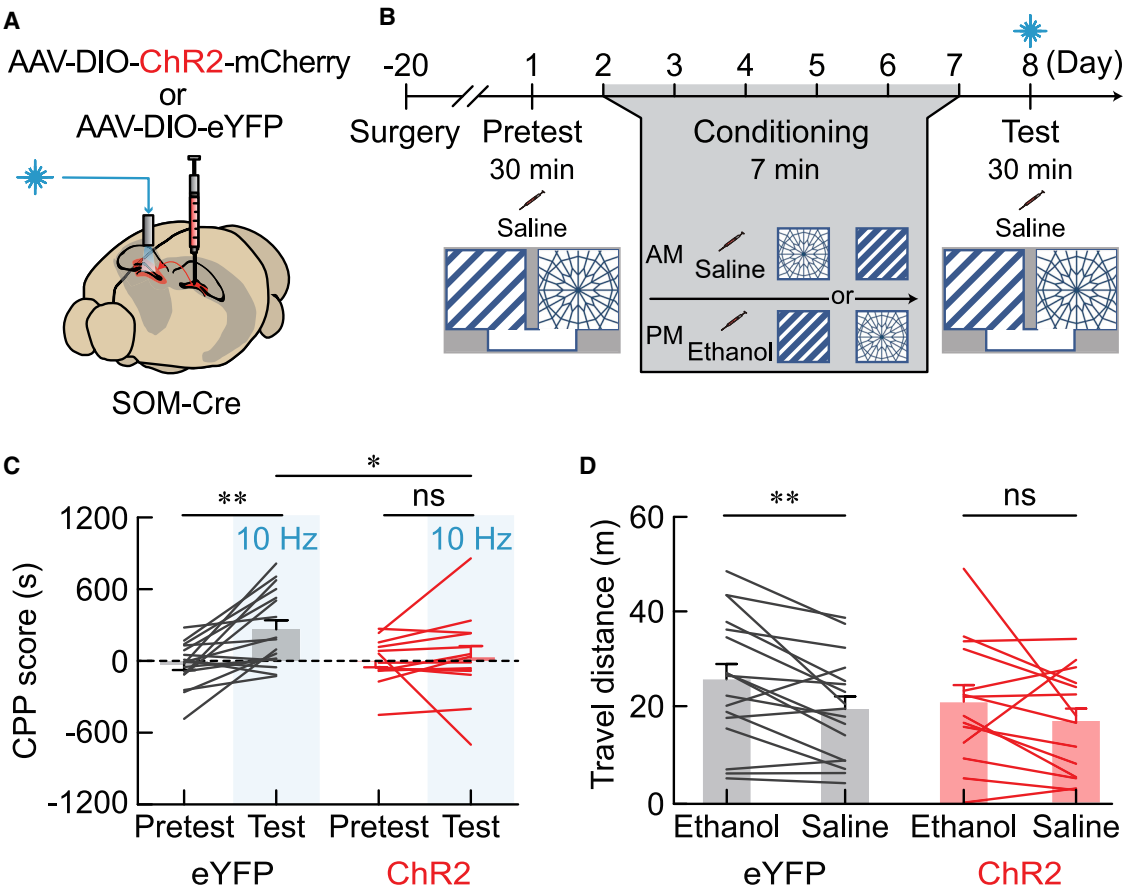

Figure 3. Stimulating SOM$^+$ cDG projections disrupts contextual memory

(A) Schematic of the viral injection (eYFP/control, 17 mice; ChR2-mCherry, 14 mice) and optical fiber implantation in SOM-Cre mice.

(B) Experimental design of the CPP test. Three weeks after surgery, mice perform the test, which comprises three sessions: a pretest session on day 1, followed by 5 conditioning days (days 2–7, day 5 is a rest day), and a test session on day 8. During the pretest and test sessions, the mice freely explore the two chambers after having received saline. During the conditioning session, the mice receive saline in the morning (AM) in the assigned non-reward chamber and ethanol in the afternoon (PM) in the assigned reward chamber. Laser stimulation at 10 Hz (9.0–9.5 mW) is delivered on the test day.

(C) CPP scores from eYFP and ChR2 mice in the pretest and test sessions. The CPP score is evaluated by subtracting the time spent in the reward chamber from that in the non-reward chamber. $p = 0.0199$, two-way analysis of variance (ANOVA) ($F_{(1,29)} = 5.844$) with Sidak correction for multiple comparisons; *$p = 0.0392$ and **$p = 0.006$.

(D) Distances traveled on the test day for eYFP and ChR2 mice in the reward and non-reward chambers. **$p < 0.01$, Wilcoxon signed-rank test.

two hemispheres. The molecular identity of these projections, namely the SOM positivity, was first reported by Melzer and colleagues (Melzer et al., 2012) and was further substantiated a few years later (Eyre and Bartos, 2019). Subsequent studies identified also PV$^+$ and calbindin$^+$ neurons that connect the left and right DG (Eyre and Bartos, 2019; Wick et al., 2017), and here we have added VIP$^+$ neurons to this repertoire of GABAergic projection neurons. A number of technical variables such as site and volume of injection preclude a direct comparison that would enable a quantitative evaluation regarding the proportion of these distinct GABAergic projections, but based on all these studies it is safe to assume that SOM$^+$ projections prevail. Hence this population became the target of our functional investigations, which does not imply, however, that the sparser PV$^+$, VIP$^+$, or calbindin$^+$ projections connecting the two DGs are of less functional significance. On the contrary, further investigations of these projections are warranted but may be technically more challenging.

We first sought to obtain information pertaining to the identity of inhibited cells in the target region. Different connectivity patterns have been reported for other GABAergic projection neurons that connect subdomains of the parahippocampal area. Thus, GABAergic neurons connecting the medial entorhinal cortex and CA1 bidirectionally target predominantly or even exclusively GABAergic neurons (Melzer et al., 2012), whereas GABAergic neurons mediating bidirectional cross talk between the subiculum and CA1 innervate both interneurons and principal cells in the target area (Francavilla et al., 2018; Sun et al., 2014). The GABAergic projection pattern between the two DGs is reminiscent of the latter connectivity pattern in that the target cells comprise interneurons and principal cells. Specifically, cDG projections inhibit several types of interneurons and principal cells. It

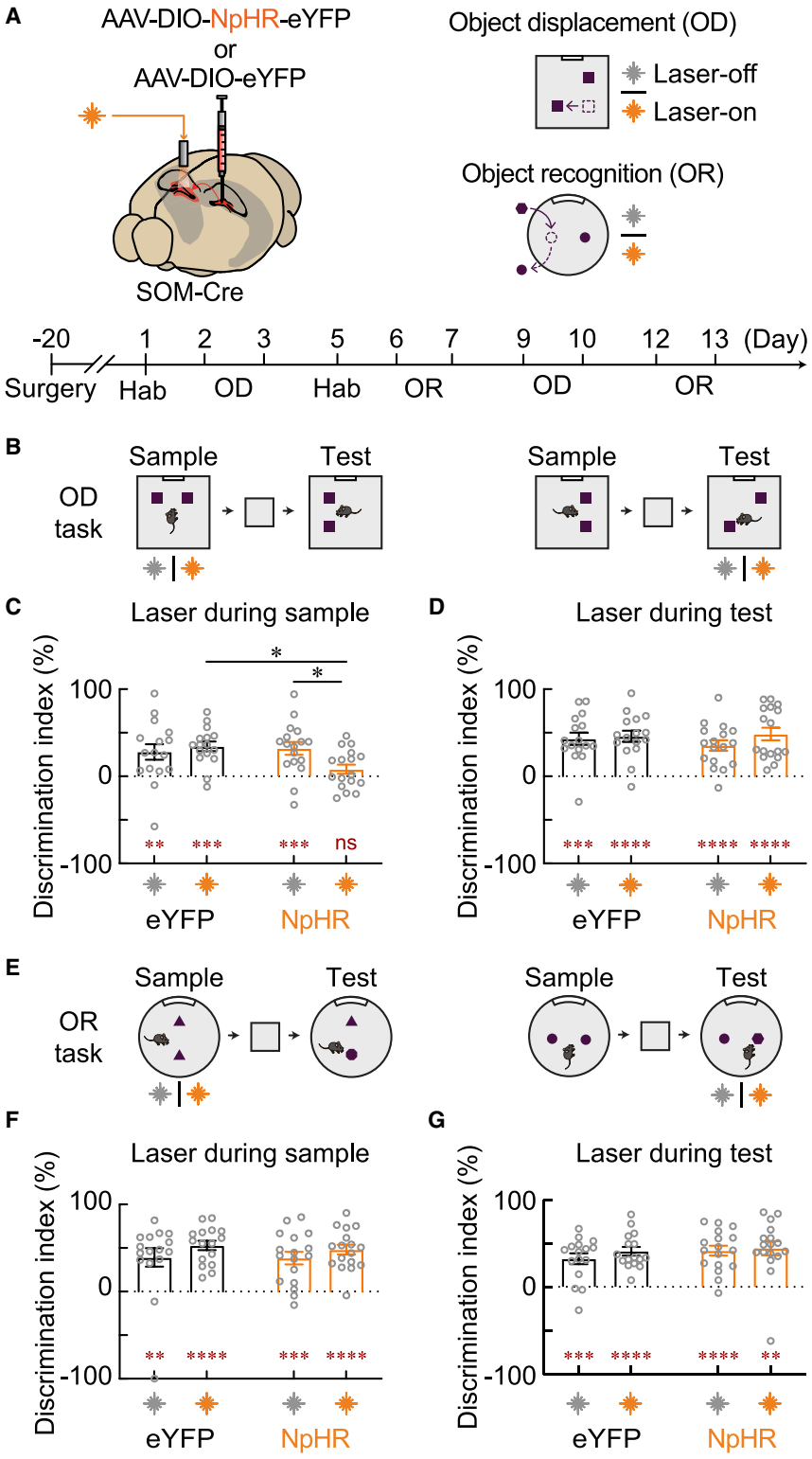

Figure 4. Silencing SOM$^+$ cDG projections during memory acquisition, but not retrieval, impairs spatial memory

(A) Top, left, schematic of the viral injection (eYFP/control, 16 mice; NpHR-eYFP, 17 mice) and optical fiber implantation in the cDG. Top, right, schematic of the object displacement (OD) and object recognition (OR) tests. The laser symbol is color coded to indicate trials with laser-off or laser-on stimulation. Bottom, OD and OR experimental timeline.

(B) Experimental design of the OD task. Left, a 589 nm laser (9.0–9.5 mW) is delivered continuously during the 10 min sample session in half of the animals on the first day, while the second half of the mice receive a sham stimulation. After 5 min resting in the rest box, the mice are placed in the apparatus with a new spatial-object configuration. The same procedure is repeated on the second day, while the group that received sham stimulus receive laser stimulation, and vice versa. Right, the mice freely explore the arena during the 10 min sample session; after 5 min resting in the rest box, a 589 nm laser is delivered continuously during the 5 min test session to half of the animals, while the second half of the mice receive a sham stimulation. This procedure is repeated on the second day with reversed laser assignment in the test trials.

(C) The discrimination index (DI) when the mice receive laser manipulation during the OD sample sessions. No difference in DI is observed in eYFP mice between laser-off and laser-on manipulations. The DIs from NpHR-eYFP mice that received laser-on treatment during the sample session are significantly lower than when the mice received laser-off treatment. Two-way ANOVA ($F_{(1, 31)} = 5.596$) with Sidak correction for multiple comparisons test, *p = 0.0231. The DI of NpHR-eYFP mice that received laser-on treatment is lower than the DI from eYFP mice, *p = 0.0192. The distribution of DIs from NpHR-eYFP mice that received laser-on treatment during the sample session does not vary from 0. Wilcoxon signed-rank test, p = 0.1459. Red asterisks refer to a one-sample Wilcoxon signed-rank test of the DIs versus chance level (0%), **p < 0.01; ***p < 0.001. Graph shows mean + SEM.

(D) The DIs when the mice receive laser manipulation during the OD test session. No difference in DIs between laser-off and laser-on manipulations is observed in the eYFP mice nor in the NpHR-eYFP mice. Two-way ANOVA ($F_{(1, 31)} = 0.7002$). Red asterisks refer to a one-sample Wilcoxon signed-rank test of the DIs versus chance level (0%), ***p < 0.001; ****p < 0.0001. Graph shows mean + SEM.

(E) Similar to (B), but object recognition task was used.

(F) The DIs when the mice receive laser manipulation during the OR sample session. There is no difference in DIs between laser-off and laser-on manipulations in the eYFP mice nor in the NpHR-eYFP mice. Two-way ANOVA ($F_{(1, 31)} = 0.0853$). Red asterisks refer to a one-sample Wilcoxon signed-rank test of the DIs versus chance level (0%), **p < 0.01; ***p < 0.001; ****p <0.0001. Graph shows mean + SEM.

(G) The DIs when the mice receive laser manipulation during the OR sample session. There is no difference in DIs between laser-off and laser-on manipulations in the eYFP mice nor in the NpHR-eYFP mice. Two-way ANOVA ($F_{(1, 31)} = 0.3307$). Red asterisks refer to a one-sample Wilcoxon signed-rank test of the DIs versus chance level (0%), **p < 0.01; ***p < 0.001; ****p < 0.0001. Graph shows mean + SEM.

(legend continued on next page)

should be emphasized, though, that axonal activation of cDG projections had a greater effect on morphologically defined interneurons in the contralateral hemisphere: both the proportion of inhibited interneurons was greater than that of principal cells and the strength of inhibition was greater on interneurons than on GCs. In view of a previous study, it may be surprising that, upon light-induced axonal activation of cDG projections, we were able to detect the inhibitory currents in distinct target neurons. Thus, Eyre and colleagues (Eyre and Bartos, 2019) characterized these very same projections anatomically, yet were unable to elicit responses in neurons of the cDG. This discrepancy is most likely technical in nature. Parsimonious explanations include any of the following: the different genotypes of the mice (GAD2-IRES-Cre in the Eyre study, SOM-IRES-Cre in our study), the different promoters driving ChR2 expression (CAG in the Eyre study and EF1a in our study), and/or the time allowed for ChR2 translation. All can result in quantitative differences in transmitter release and ChR2 expression.

Although SOM$^+$ cDG-projecting neurons directly innervate excitatory and dendrite-targeting inhibitory neurons but not soma-targeting inhibitory fast-spiking cells, the *in vivo* recordings revealed that the modulatory effect was most notable in narrow-waveform, fast-spiking cells. The electrophysiological results enable several inferences regarding the recruitment and sequential activation of DG neurons. To recapitulate, based on the differential modulatory effects and latencies, we distinguished I_E, I_L, and E responsive cells. The latencies of E responsive cells were between I_E and I_L, suggesting that E and I_L responses corresponded to sequentially triggered polysynaptic responses. This assumption was further corroborated by investigating the cell types in the three responsive groups. Thus, I_E responses were observed predominately in wide-waveform inhibitory neurons that in turn would have a disinhibitory effect in E responsive cells that would then trigger I_L responses in two ways: interneurons with E response would further suppress I_L (Halasy and Somogyi, 1993; Savanthrapadian et al., 2014), and excitatory cells with E response would cause feedforward inhibition (Buzsáki and Czéh, 1981; Buzsáki and Eidelberg, 1981; Bilkey and Goddard 1987; Hsu et al., 2016). Indeed, we identified interneuron-like cells and also spatial selective cells in the E responsive group.

The number of cells recruited in a memory trace in the hippocampus is largely controlled by interneurons (Donato et al., 2013; Halasy and Somogyi, 1993; Lee et al., 2016; Lovett-Barron et al., 2014; Royer et al., 2012; Stefanelli et al., 2016). Several studies have shown that silencing or activating PV$^+$ or SOM$^+$ cells during memory acquisition, retrieval, or consolidation impairs associated behavioral outcomes in different behavioral paradigms (Deng et al., 2019; Morales et al., 2021; Murray et al., 2011; Xia et al., 2017). Therefore, we investigated whether manipulation of cDG projections would have an impact on memory acquisition and retrieval. The hippocampus is known for its role in processing both spatial and non-spatial memory (Barker and Warburton, 2011; Ennaceur and Delacour, 1988; Mumby et al., 2002), which we assessed here by the OD and OR behavioral test, respectively. As designed, and in particular with the precise inactivation during the sample or test phase, we were able to determine whether cDG projections were involved in memory acquisition and/or retrieval in the two types of memory. Thus, our results support the notion that in the spatial OD task cDG projections were relevant for memory acquisition but not memory retrieval. This is reminiscent of what was reported by Morales et al. (2021). The authors reported a similar phenotype upon bilateral silencing of SOM$^+$ neurons in the DG, raising the question as to the exact contribution of SOM$^+$ interneurons and SOM$^+$ cDG projection neurons. Our study further demonstrated that silencing cDG projection during either the sample or the test phase did not affect OR. This is in line with previous studies showing that the hippocampus did not support non-spatial memory when tested like here, with short delays in the OR task (Barker and Warburton, 2011; Cohen et al., 2013; Hammond et al., 2004). These studies, however, revealed the role of the hippocampus in OR memory at long delays (24 h). Interestingly, while cDG projections do not support retrieval of OD or OR memory, they do play a role in other forms of long-term memory, such as in the retrieval of an already established context-reward memory.

The increasing number of "novel" GABAergic projections connecting many cortical and subcortical brain areas clearly raise the question as to the function of these neurons. It remains a daunting task to associate these projections with defined functions, as the few existing functional studies clearly point to selective functions for each of these projections. For instance, two GABAergic projections from the septum to the medial entorhinal cortex differentially affect the activity in the target area and the behavior of the animals in memory tasks (Schlesiger et al., 2021). Similarly, two defined GABAergic projections from the motor cortex to the striatum differentially affect locomotion in freely moving animals (Melzer et al., 2017). However, conclusive answers regarding the function of defined GABAergic projections will remain a challenge and await focused studies on the function of these neurons during specific tasks.

In sum, in this study we investigated SOM$^+$ cDG projections connecting the DG in the two hemispheres. We combined viral tracing and electrophysiological recordings *in vitro* to determine the identity of the target neurons, as well as *in vivo* recordings and behavioral investigations to obtain insight into the modulatory effect that these projections exert at the functional level. Together, our results demonstrate that, despite the sparse nature of SOM$^+$ cDG projections, modulating their activity during memory encoding or retrieval causes a disruption in memory processing capable of altering behavior.

Limitations of the study

In this study we focused on cDG-projecting SOM$^+$ cells because they were more numerous than PV$^+$ or VIP$^+$ neurons projecting from one DG to the other. This may not necessarily mean that they have less or no function. Furthermore, and more important, in the absence of specific markers for GABAergic projection neurons, it was not possible to differentially label cDG-projecting SOM$^+$ cells and SOM$^+$ interneurons. Thus, we were constrained to activate or inhibit axons of cDG-projecting SOM$^+$ cells unilaterally. On one hand, this could be viewed as a drawback in the context of the behavioral studies, but on the other, we predict an even stronger phenotype upon bilateral manipulation.

STAR★METHODS

Detailed methods are provided in the online version of this paper and include the following:

- KEY RESOURCES TABLE
- RESOURCE AVAILABILITY
  - Lead contact
  - Materials availability
  - Data and code availability
- EXPERIMENTAL MODEL AND SUBJECT DETAILS
- METHOD DETAILS
  - Stereotaxic viral injections and implantations
  - Slice electrophysiology
  - Neuron-labeling and reconstruction
  - *In vivo* unit recordings
  - Criteria to determine responsive cells
  - Physiological features of neurons recorded *in vivo*
  - Criteria to define spatial-selective cells
  - Immunohistochemistry
  - Conditioned place preference test
  - Object displacement (OD) and object recognition (OR) task
- QUANTIFICATION AND STATISTICAL ANALYSIS

SUPPLEMENTAL INFORMATION

Supplemental information can be found online at https://doi.org/10.1016/j.celrep.2022.110831.

ACKNOWLEDGMENTS

We thank D. Engel and S.C. Lin for commenting on earlier versions of the manuscript and all of the Lien lab members for insightful discussions. This work was financially supported by the Brain Research Center, National Yang Ming Chiao Tung University, from the Featured Areas Research Center Program within the framework of the Higher Education Sprout Project of the Ministry of Education, National Health Research Institutes (NHRI-EX108-10814NI), Ministry of Science and Technology (Dragon Gate Program 108-2911-I-010-504; Shackleton Scholar Program 108-2638-B-010-002-MY2), in Taiwan, and by Baden-Württemberg Stiftung (BWST_ISF2018-036) to H.M.

AUTHOR CONTRIBUTIONS

T.Y.Y., M.I.S., D.A.A.M., H.M., and C.C.L. designed the experiments. T.Y.Y. and X.H. executed the experiments. T.Y.Y. analyzed the data. T.Y.Y., H.M., and C.C.L. wrote the paper. H.M. and C.C.L. acquired the funding.

DECLARATION OF INTERESTS

The authors declare no competing interests.

Received: November 12, 2020
Revised: November 17, 2021
Accepted: April 27, 2022
Published: May 17, 2022

REFERENCES

Amaral, D.G., Insausti, R., and Campbell, M.J. (1988). Distribution of somatostatin immunoreactivity in the human dentate gyrus. J. Neurosci. *8*, 3306–3316. https://doi.org/10.1523/jneurosci.08-09-03306.1988.

Amaral, D.G., Scharfman, H.E., and Lavenex, P. (2007). The dentate gyrus: fundamental neuroanatomical organization (dentate gyrus for dummies). Prog. Brain Res. *163*, 3–22. https://doi.org/10.1016/s0079-6123(07)63001-5.

Anderson, J.S., Carandini, M., and Ferster, D. (2000). Orientation tuning of input conductance, excitation, and inhibition in cat primary visual cortex. J. Neurophysiol. *84*, 909–926. https://doi.org/10.1152/jn.2000.84.2.909.

Atallah, B.V., and Scanziani, M. (2009). Instantaneous modulation of gamma oscillation frequency by balancing excitation with inhibition. Neuron *62*, 566–577. https://doi.org/10.1016/j.neuron.2009.04.027.

Bakst, I., Avendano, C., Morrison, J.H., and Amaral, D.G. (1986). An experimental analysis of the origins of somatostatin-like immunoreactivity in the dentate gyrus of the rat. J. Neurosci. *6*, 1452–1462. https://doi.org/10.1523/jneurosci.06-05-01452.1986.

Barker, G.R.I., and Warburton, E.C. (2011). When is the hippocampus involved in recognition memory? J. Neurosci. *31*, 10721–10731. https://doi.org/10.1523/jneurosci.6413-10.2011.

Bartos, M., Vida, I., and Jonas, P. (2007). Synaptic mechanisms of synchronized gamma oscillations in inhibitory interneuron networks. Nat. Rev. Neurosci. *8*, 45–56. https://doi.org/10.1038/nrn2044.

Basu, J., Zaremba, J.D., Cheung, S.K., Hitti, F.L., Zemelman, B.V., Losonczy, A., and Siegelbaum, S.A. (2016). Gating of hippocampal activity, plasticity, and memory by entorhinal cortex long-range inhibition. Science *351*, aaa5694. https://doi.org/10.1126/science.aaa5694.

Bhatia, A., Moza, S., and Bhalla, U.S. (2019). Precise excitation-inhibition balance controls gain and timing in the hippocampus. eLife *8*, e43415. https://doi.org/10.7554/eLife.43415.

Bilkey, D.K., and Goddard, G.V. (1987). Septohippocampal and commissural pathways antagonistically control inhibitory interneurons in the dentate gyrus. Brain Res. *405*, 320–325. https://doi.org/10.1016/0006-8993(87)90301-5.

Buzsáki, G., and Czéh, G. (1981). Commissural and perforant path interactions in the rat hippocampus. Field potentials and unitary activity. Exp. Brain Res. *43*, 429–438. https://doi.org/10.1007/BF00238387.

Buzsáki, G., and Eidelberg, E. (1981). Commissural projection to the dentate gyrus of the rat: evidence for feed-forward inhibition. Brain Res. *230*, 346–350. https://doi.org/10.1016/0006-8993(81)90413-3.

Caputi, A., Melzer, S., Michael, M., and Monyer, H. (2013). The long and short of GABAergic neurons. Curr. Opin. Neurobiol. *23*, 179–186. https://doi.org/10.1016/j.conb.2013.01.021.

Cohen, S.J., Munchow, A.H., Rios, L.M., Zhang, G., Ásgeirsdóttir, H.N., and Stackman, R.W., Jr. (2013). The rodent hippocampus is essential for nonspatial object memory. Curr. Biol. *23*, 1685–1690. https://doi.org/10.1016/j.cub.2013.07.002.

Deadwyler, S.A., West, J.R., Cotman, C.W., and Lynch, G.S. (1975). A neurophysiological analysis of commissural projections to dentate gyrus of the rat. J. Neurophysiol. *38*, 167–184. https://doi.org/10.1152/jn.1975.38.1.167.

Deng, X., Gu, L., Sui, N., Guo, J., and Liang, J. (2019). Parvalbumin interneuron in the ventral hippocampus functions as a discriminator in social memory. Proc. Natl. Acad. Sci. U S A *116*, 16583–16592. https://doi.org/10.1073/pnas.1819133116.

Donato, F., Rompani, S.B., and Caroni, P. (2013). Parvalbumin-expressing basket-cell network plasticity induced by experience regulates adult learning. Nature *504*, 272–276. https://doi.org/10.1038/nature12866.

Ennaceur, A., and Delacour, J. (1988). A new one-trial test for neurobiological studies of memory in rats. 1: behavioral data. Behav. Brain Res. *31*, 47–59. https://doi.org/10.1016/0166-4328(88)90157-x.

Espinoza, C., Guzman, S.J., Zhang, X., and Jonas, P. (2018). Parvalbumin(+) interneurons obey unique connectivity rules and establish a powerful lateral-inhibition microcircuit in dentate gyrus. Nat. Commun. *9*, 4605. https://doi.org/10.1038/s41467-018-06899-3.

Eyre, M.D., and Bartos, M. (2019). Somatostatin-expressing interneurons form axonal projections to the contralateral hippocampus. Front. Neural Circuits *13*, 56. https://doi.org/10.3389/fncir.2019.00056.

Francavilla, R., Villette, V., Luo, X., Chamberland, S., Muñoz-Pino, E., Camiré, O., Wagner, K., Kis, V., Somogyi, P., and Topolnik, L. (2018). Connectivity and network state-dependent recruitment of long-range VIP-GABAergic neurons in the mouse hippocampus. Nat. Commun. *9*, 5043. https://doi.org/10.1038/s41467-018-07162-5.

Fujise, N., and Kosaka, T. (1999). Mossy cells in the mouse dentate gyrus: identification in the dorsal hilus and their distribution along the dorsoventral axis. Brain Res. *816*, 500–511. https://doi.org/10.1016/s0006-8993(98)01202-5.

Gil, M., Ancau, M., Schlesiger, M.I., Neitz, A., Allen, K., De Marco, R.J., and Monyer, H. (2018). Impaired path integration in mice with disrupted grid cell firing. Nat. Neurosci. *21*, 81–91. https://doi.org/10.1038/s41593-017-0039-3.

GoodSmith, D., Chen, X., Wang, C., Kim, S.H., Song, H., Burgalossi, A., Christian, K.M., and Knierim, J.J. (2017). Spatial representations of granule cells and mossy cells of the dentate gyrus. Neuron *93*, 677–690.e5. https://doi.org/10.1016/j.neuron.2016.12.026.

GoodSmith, D., Lee, H., Neunuebel, J.P., Song, H., and Knierim, J.J. (2019). Dentate gyrus mossy cells share a role in pattern separation with dentate granule cells and proximal CA3 pyramidal cells. J. Neurosci. *39*, 9570–9584. https://doi.org/10.1523/jneurosci.0940-19.2019.

Halasy, K., and Somogyi, P. (1993). Subdivisions in the multiple GABAergic innervation of granule cells in the dentate gyrus of the rat hippocampus. Eur. J. Neurosci. *5*, 411–429. https://doi.org/10.1111/j.1460-9568.1993.tb00508.x.

Hammond, R.S., Tull, L.E., and Stackman, R.W. (2004). On the delay-dependent involvement of the hippocampus in object recognition memory. Neurobiol. Learn. Mem. *82*, 26–34. https://doi.org/10.1016/j.nlm.2004.03.005.

Robert Heale, V., and Vanderwolf, C.H. (1994). Dentate gyrus and olfactory bulb responses to olfactory and noxious stimulation in urethane anaesthetized rats. Brain Res. *652*, 235–242. https://doi.org/10.1016/0006-8993(94)90232-1.

Hippenmeyer, S., Vrieseling, E., Sigrist, M., Portmann, T., Laengle, C., Ladle, D.R., and Arber, S. (2005). A developmental switch in the response of DRG neurons to ETS transcription factor signaling. PLoS Biol. *3*, e159. https://doi.org/10.1371/journal.pbio.0030159.

Hsu, T.T., Lee, C.T., Tai, M.H., and Lien, C.C. (2016). Differential recruitment of dentate gyrus interneuron types by commissural versus perforant pathways. Cereb. Cortex *26*, 2715–2727. https://doi.org/10.1093/cercor/bhv127.

Huckleberry, K.A., Kane, G.A., Mathis, R.J., Cook, S.G., Clutton, J.E., and Drew, M.R. (2015). Behavioral experience induces zif268 expression in mature granule cells but suppresses its expression in immature granule cells. Front. Syst. Neurosci. *9*, 118. https://doi.org/10.3389/fnsys.2015.00118.

Hurst, J.L., and West, R.S. (2010). Taming anxiety in laboratory mice. Nat. Methods *7*, 825–826. https://doi.org/10.1038/nmeth.1500.

Jinno, S., Klausberger, T., Marton, L.F., Dalezios, Y., Roberts, J.D.B., Fuentealba, P., Bushong, E.A., Henze, D., Buzsáki, G., and Somogyi, P. (2007). Neuronal diversity in GABAergic long-range projections from the hippocampus. J. Neurosci. *27*, 8790–8804. https://doi.org/10.1523/jneurosci.1847-07.2007.

Jonas, P., and Lisman, J. (2014). Structure, function, and plasticity of hippocampal dentate gyrus microcircuits. Front. Neural Circuits *8*, 107. https://doi.org/10.3389/fncir.2014.00107.

Kirschen, G.W., Shen, J., Tian, M., Schroeder, B., Wang, J., Man, G., Wu, S., and Ge, S. (2017). Active dentate granule cells encode experience to promote the addition of adult-born hippocampal neurons. J. Neurosci. *37*, 4661–4678. https://doi.org/10.1523/jneurosci.3417-16.2017.

Kornienko, O., Latuske, P., Bassler, M., Kohler, L., and Allen, K. (2018). Non-rhythmic head-direction cells in the parahippocampal region are not constrained by attractor network dynamics. eLife *7*, e35949. https://doi.org/10.7554/elife.35949.

Lee, C.T., Kao, M.H., Hou, W.H., Wei, Y.T., Chen, C.L., and Lien, C.C. (2016). Causal evidence for the role of specific GABAergic interneuron types in entorhinal recruitment of dentate granule cells. Sci. Rep. *6*, 36885. https://doi.org/10.1038/srep36885.

Lein, E.S., Hawrylycz, M.J., Ao, N., Ayres, M., Bensinger, A., Bernard, A., Boe, A.F., Boguski, M.S., Brockway, K.S., Byrnes, E.J., et al. (2007). Genome-wide atlas of gene expression in the adult mouse brain. Nature *445*, 168–176. https://doi.org/10.1038/nature05453.

Lenck-Santini, P.-P., Rivard, B., Muller, R.U., and Poucet, B. (2005). Study of CA1 place cell activity and exploratory behavior following spatial and nonspatial changes in the environment. Hippocampus *15*, 356–369. https://doi.org/10.1002/hipo.20060.

Leutgeb, J.K., Leutgeb, S., Moser, M.-B., and Moser, E.I. (2007). Pattern separation in the dentate gyrus and CA3 of the hippocampus. Science *315*, 961–966. https://doi.org/10.1126/science.1135801.

Lovett-Barron, M., Kaifosh, P., Kheirbek, M.A., Danielson, N., Zaremba, J.D., Reardon, T.R., Turi, G.F., Hen, R., Zemelman, B.V., and Losonczy, A. (2014). Dendritic inhibition in the hippocampus supports fear learning. Science *343*, 857–863. https://doi.org/10.1126/science.1247485.

Mathis, A., Mamidanna, P., Cury, K.M., Abe, T., Murthy, V.N., Mathis, M.W., and Bethge, M. (2018). DeepLabCut: markerless pose estimation of user-defined body parts with deep learning. Nat. Neurosci. *21*, 1281–1289. https://doi.org/10.1038/s41593-018-0209-y.

McNaughton, B.L., and Barnes, C.A. (1977). Physiological identification and analysis of dentate granule cell responses to stimulation of the medial and lateral perforant pathways in the rat. J. Comp. Neurol. *175*, 439–454. https://doi.org/10.1002/cne.901750404.

McNaughton, B.L., and Morris, R.G.M. (1987). Hippocampal synaptic enhancement and information storage within a distributed memory system. Trends Neurosci. *10*, 408–415. https://doi.org/10.1016/0166-2236(87)90011-7.

Melzer, S., Michael, M., Caputi, A., Eliava, M., Fuchs, E.C., Whittington, M.A., and Monyer, H. (2012). Long-range-projecting GABAergic neurons modulate inhibition in hippocampus and entorhinal cortex. Science *335*, 1506–1510. https://doi.org/10.1126/science.1217139.

Melzer, S., Gil, M., Koser, D.E., Michael, M., Huang, K.W., and Monyer, H. (2017). Distinct corticostriatal GABAergic neurons modulate striatal output neurons and motor activity. Cell Rep. *19*, 1045–1055. https://doi.org/10.1016/j.celrep.2017.04.024.

Melzer, S., and Monyer, H. (2020). Diversity and function of corticopetal and corticofugal GABAergic projection neurons. Nat. Rev. Neurosci. *21*, 499–515. https://doi.org/10.1038/s41583-020-0344-9.

Morales, C., Morici, J.F., Espinosa, N., Sacson, A., Lara-Vasquez, A., García-Pérez, M.A., Bekinschtein, P., Weisstaub, N.V., and Fuentealba, P. (2021). Dentate gyrus somatostatin cells are required for contextual discrimination during episodic memory encoding. Cereb. Cortex *31*, 1046–1059. https://doi.org/10.1093/cercor/bhaa273.

Morrison, J.H., Benoit, R., Magistretti, P.J., Ling, N., and Bloom, F.E. (1982). Immunohistochemical distribution of pro-somatostatin-related peptides in hippocampus. Neurosci. Lett. *34*, 137–142. https://doi.org/10.1016/0304-3940(82)90165-3.

Mumby, D.G., Gaskin, S., Glenn, M.J., Schramek, T.E., and Lehmann, H. (2002). Hippocampal damage and exploratory preferences in rats: memory for objects, places, and contexts. Learn. Mem. *9*, 49–57. https://doi.org/10.1101/lm.41302.

Murray, A.J., Sauer, J.F., Riedel, G., McClure, C., Ansel, L., Cheyne, L., Bartos, M., Wisden, W., and Wulff, P. (2011). Parvalbumin-positive CA1 interneurons are required for spatial working but not for reference memory. Nat. Neurosci. *14*, 297–299. https://doi.org/10.1038/nn.2751.

Myatt, D.R., Hadlington, T., Ascoli, G.A., and Nasuto, S.J. (2012). Neuromantic – from semi-manual to semi-automatic reconstruction of neuron morphology. Front. Neuroinform. *6*, 4. https://doi.org/10.3389/fninf.2012.00004.

Neunuebel, J.P., and Knierim, J.J. (2014). CA3 retrieves coherent representations from degraded input: direct evidence for CA3 pattern completion and dentate gyrus pattern separation. Neuron *81*, 416–427. https://doi.org/10.1016/j.neuron.2013.11.017.

O'Keefe, J. (1999). Do hippocampal pyramidal cells signal non-spatial as well as spatial information? Hippocampus *9*, 352–364. https://doi.org/10.1002/(sici)1098-1063(1999)9:4<352::aid-hipo3>3.0.co;2-1.

Okun, M., and Lampl, I. (2008). Instantaneous correlation of excitation and inhibition during ongoing and sensory-evoked activities. Nat. Neurosci. *11*, 535–537. https://doi.org/10.1038/nn.2105.

Olton, D.S., Becker, J.T., and Handelmann, G.E. (1979). Hippocampus, space, and memory. Behav. Brain Sci. *2*, 313–322. https://doi.org/10.1017/s0140525x00062713.

Ribak, C.E., Seress, L., Peterson, G.M., Seroogy, K.B., Fallon, J.H., and Schmued, L.C. (1986). A GABAergic inhibitory component within the hippocampal commissural pathway. J. Neurosci. *6*, 3492–3498. https://doi.org/10.1523/jneurosci.06-12-03492.1986.

Rossant, C., Kadir, S.N., Goodman, D.F.M., Schulman, J., Hunter, M.L.D., Saleem, A.B., Grosmark, A., Belluscio, M., Denfield, G.H., Ecker, A.S., et al. (2016). Spike sorting for large, dense electrode arrays. Nat. Neurosci. *19*, 634–641. https://doi.org/10.1038/nn.4268.

Royer, S., Zemelman, B.V., Losonczy, A., Kim, J., Chance, F., Magee, J.C., and Buzsáki, G. (2012). Control of timing, rate and bursts of hippocampal place cells by dendritic and somatic inhibition. Nat. Neurosci. *15*, 769–775. https://doi.org/10.1038/nn.3077.

Savanthrapadian, S., Meyer, T., Elgueta, C., Booker, S.A., Vida, I., and Bartos, M. (2014). Synaptic properties of SOM- and CCK-expressing cells in dentate gyrus interneuron networks. J. Neurosci. *34*, 8197–8209. https://doi.org/10.1523/jneurosci.5433-13.2014.

Schindelin, J., Arganda-Carreras, I., Frise, E., Kaynig, V., Longair, M., Pietzsch, T., Preibisch, S., Rueden, C., Saalfeld, S., Schmid, B., et al. (2012). Fiji: an open-source platform for biological-image analysis. Nat. Methods *9*, 676–682. https://doi.org/10.1038/nmeth.2019.

Schlesiger, M.I., Ruff, T., MacLaren, D.A.A., Barriuso-Ortega, I., Saidov, K.M., Yen, T.Y., and Monyer, H. (2021). Two septal-entorhinal GABAergic projections differentially control coding properties of spatially tuned neurons in the medial entorhinal cortex. Cell Rep. *34*, 108801. https://doi.org/10.1016/j.celrep.2021.108801.

Senzai, Y., and Buzsáki, G. (2017). Physiological properties and behavioral correlates of hippocampal granule cells and mossy cells. Neuron *93*, 691–704.e5. https://doi.org/10.1016/j.neuron.2016.12.011.

Sik, A., Penttonen, M., and Buzsáki, G. (1997). Interneurons in the hippocampal dentate gyrus: an in vivo intracellular study. Eur. J. Neurosci. *9*, 573–588. https://doi.org/10.1111/j.1460-9568.1997.tb01634.x.

Skaggs, W.E., McNaughton, B.L., Gothard, K.M., and Markus, E.J. (1993). An information-theoretic approach to deciphering the hippocampal code. In Advances in Neural Information Processing Systems, C.L. Giles, S.J. Hanson, and J.D. Cowan, eds. (Morgan Kaufman), pp. 1030–1037.

Sloviter, R.S., and Brisman, J.L. (1995). Lateral inhibition and granule cell synchrony in the rat hippocampal dentate gyrus. J. Neurosci. *15*, 811–820. https://doi.org/10.1523/jneurosci.15-01-00811.1995.

Stefanelli, T., Bertollini, C., Luscher, C., Muller, D., and Mendez, P. (2016). Hippocampal somatostatin interneurons control the size of neuronal memory ensembles. Neuron *89*, 1074–1085. https://doi.org/10.1016/j.neuron.2016.01.024.

Sun, Y., Nguyen, A.Q., Nguyen, J.P., Le, L., Saur, D., Choi, J., Callaway, E.M., and Xu, X. (2014). Cell-type-specific circuit connectivity of hippocampal CA1 revealed through Cre-dependent rabies tracing. Cell Rep. *7*, 269–280. https://doi.org/10.1016/j.celrep.2014.02.030.

Tamamaki, N., Yanagawa, Y., Tomioka, R., Miyazaki, J.I., Obata, K., and Kaneko, T. (2003). Green fluorescent protein expression and colocalization with calretinin, parvalbumin, and somatostatin in the GAD67-GFP knock-in mouse. J. Comp. Neurol. *467*, 60–79. https://doi.org/10.1002/cne.10905.

Taniguchi, H., He, M., Wu, P., Kim, S., Paik, R., Sugino, K., Kvitsiani, D., Fu, Y., Lu, J., Lin, Y., et al. (2011). A resource of Cre driver lines for genetic targeting of GABAergic neurons in cerebral cortex. Neuron *71*, 995–1013. https://doi.org/10.1016/j.neuron.2011.12.010.

Tulving, E., and Markowitsch, H.J. (1998). Episodic and declarative memory: role of the hippocampus. Hippocampus *8*, 198–204. https://doi.org/10.1002/(sici)1098-1063(1998)8:3<198::aid-hipo2>3.0.co;2-g.

van Strien, N.M., Cappaert, N.L.M., and Witter, M.P. (2009). The anatomy of memory: an interactive overview of the parahippocampal-hippocampal network. Nat. Rev. Neurosci. *10*, 272–282. https://doi.org/10.1038/nrn2614.

Wan, X.C.S., Trojanowski, J.Q., and Gonatas, J.O. (1982). Cholera toxin and wheat germ agglutinin conjugates as neuroanatomical probes: their uptake and clearance, transganglionic and retrograde transport and sensitivity. Brain Res. *243*, 215–224. https://doi.org/10.1016/0006-8993(82)90244-x.

Wang, K.-Y., Wu, J.-W., Cheng, J.-K., Chen, C.-C., Wong, W.-Y., Averkin, R.-G., Tamás, G., Nakazawa, K., and Lien, C.-C. (2021). Elevation of hilar mossy cell activity suppresses hippocampal excitability and avoidance behavior. Cell Rep. *36*, 109702. https://doi.org/10.1016/j.celrep.2021.109702.

Christenson Wick, Z., Leintz, C.H., Xamonthiene, C., Huang, B.H., and Krook-Magnuson, E. (2017). Axonal sprouting in commissurally projecting parvalbumin-expressing interneurons. J. Neurosci. Res. *95*, 2336–2344. https://doi.org/10.1002/jnr.24011.

Wiener, S.I., Paul, C.A., and Eichenbaum, H. (1989). Spatial and behavioral correlates of hippocampal neuronal activity. J. Neurosci. *9*, 2737–2763. https://doi.org/10.1523/jneurosci.09-08-02737.1989.

Xia, F., Richards, B.A., Tran, M.M., Josselyn, S.A., Takehara-Nishiuchi, K., and Frankland, P.W. (2017). Parvalbumin-positive interneurons mediate neocortical-hippocampal interactions that are necessary for memory consolidation. eLife *6*, e27868. https://doi.org/10.7554/elife.27868.

Yassa, M.A., and Stark, C.E. (2011). Pattern separation in the hippocampus. Trends Neurosci. *34*, 515–525. https://doi.org/10.1016/j.tins.2011.06.006.

STAR★METHODS

KEY RESOURCES TABLE

REAGENT or RESOURCE	SOURCE	IDENTIFIER
Antibodies		
Rabbit Polyclonal anti-DsRed	Clontech Living Colors®	Cat# 632496; RRID:AB_10013483
Rat Monoclonal anti-somatostatin	Millipore	Cat# MAB354; RRID:AB_2255365
Rabbit Polyclonal anti-GluR2/3	Millipore	Cat# AB1506; RRID:AB_90710
Bacterial and virus strains		
AAV1-DIO-ChR2(H134R)-mCherry	Addgene	RRID:Addgene_37082
AAV1-DIO-eYFP	Addgene	RRID:Addgene_27056
AAV5-DIO-eYFP	Addgene	RRID:Addgene_50462
AAV5-DIO-ChR2(H134R)-eYFP	UNC vector core	RRID:Addgene_55639
AAV5-DIO-eNpHR3.0-eYFP	Addgene	RRID:Addgene_26966
AAV5-hSyn-DIO-hM4D(Gi)-mCherry	Addgene	RRID:Addgene_44362
Chemicals, peptides, and recombinant proteins		
SR 95531 hydrobromide (gabazine)	Tocris	Cat# 1262
Kynurenic acid	Sigma-Aldrich	Cat# K3375
Clozapine N-oxide	Sigma-Aldrich	Cat# C0832
Biocytin	Invitrogen	Cat# B-1592
Experimental models: Organisms/strains		
Mouse: GAD2-Cre	Tamamaki et al., 2003	N/A
Mouse: SOM-Cre	Melzer et al., 2012	N/A
Mouse: SST-Cre	Jackson lab; Taniguchi et al., 2011	RRID: IMSR_JAX:013044
Mouse: PV-Cre	Hippenmeyer et al., 2005	N/A
Mouse: VIP-Cre	Jackson lab	RRID: IMSR_JAX:010908
Software and algorithms		
Adobe Illustrator	Adobe	https://www.adobe.com/
Clampfit 10.2	Molecular Devices	https://www.moleculardevices.com
EthoVision XT13	Noldus	http://www.noldus.com
Fiji	Schindelin et al., 2012	https://imagej.net/Fiji
GraphPad Prism 8	GraphPad	https://www.graphpad.com
KlustaKwik	Rossant et al., 2016	https://github.com/klusta-team/klustakwik
Klusters	Lynn Hazan, Buzsáki lab	N/A
Ktan	http://github.com/kevin-allen/ktan	N/A
Laser_stimulation	http://github.com/kevin-allen/laser_stimulation	N/A
Neuromantic 1.6.3	University of Reading	https://www.reading.ac.uk/neuromantic/body_index.php
Positrack	http://github.com/kevin-allen/positrack	N/A
R	http://cran.r-project.org	N/A
Relectro package	http://github.com/kevin-allen/relectro	N/A
DeepLabCut	http://github.com/DeepLabCut/DeepLabCut	N/A
Other		
4 tetrode microdrive	Axona	MDR-16TSS1
Tungsten wire 12 μm	California Fine Wire Company	EW-12T
Intan RHD2000 USB Interface Board	Intan Technologies	RHD2000
16-Channel Amplifier Board	Intan Technologies	RHD2132

RESOURCE AVAILABILITY

Lead contact

Further information and requests for resources may be directed to and will be fulfilled by the Lead Contact, Prof. Dr. Hannah Monyer (h.monyer@dkfz-heidelberg.de).

Materials availability

This study did not generate new unique reagents.

Data and code availability

All data reported in this paper will be shared by the lead contact upon request. Any additional information required to reanalyze the data reported in this paper is available from the lead contact upon request. This paper does not report original code.

EXPERIMENTAL MODEL AND SUBJECT DETAILS

All animals were handled in accordance with the European and Institutional Guidelines for the Care and Use of Laboratory Animals. The protocols were approved by the Institutional Animal Care and Use Committee of National Yang Ming Chiao Tung University and Regierungspraesidium Karlsruhe, Germany. We used glutamate decarboxylase 2 (GAD2)-Cre (Tamamaki et al., 2003), parvalbumin (PV)-Cre (Hippenmeyer et al., 2005), vasoactive intestinal polypeptide (VIP)-Cre (Jackson lab, stock no. 010908; Taniguchi et al., 2011), and somatostatin (SOM)-Cre (Melzer et al., 2012) lines for circuit mapping. Two mouse lines with Cre expression in SOM-positive neurons were used because experiments were carried out at two institutions where these lines were already established. Thus, patch-clamp recordings were performed in the lab of Dr. Lien in Taipei, while *in vivo* recordings and behavioral studies were performed in the lab of Dr. Monyer in Heidelberg. For patch-clamp recordings, we used somatostatin (SST)-Cre mice (Jackson lab, stock no. 013044; Taniguchi et al., 2011). For *in vivo* recordings and behavioral experiments we used SOM-Cre mice. Animals of both sexes (3–6 months old) were used for slice recordings, but only male mice were used for *in vivo* recordings and behavioral experiments. All mice were kept under 12h light/12h dark cycle, and all the experiments were carried out during the light portion of the cycle. To motivate mice to forage for food reward, in the random foraging *in vivo* electrophysiological experiments mice were maintained on food deprivation at a bodyweight above 85% of their free-food weight. For all other experiments, mice had food and water *ad libitum* in their home cage.

METHOD DETAILS

Stereotaxic viral injections and implantations

Mice (postnatal day $\geq$ 30) were anesthetized in an induction chamber and placed in a stereotaxic frame (David Kopf Instruments) with 0.5%–2% (v/v) isoflurane (Halocarbon Laboratories) airflow. A homeothermic warming plate (Physitemp Instrument Inc. or FMI GmbH, TKM-0904) was used to maintain a constant body temperature. After securing the head with ear bars, 75% ethanol was used to disinfect the surgical area, and the eyes were protected with an ophthalmic gel. A midline scalp incision (1.5 cm) and small craniotomies were made based on the following coordinates with reference to bregma: anteroposterior, -2 mm; mediolateral, 1.2 mm. Viruses were delivered through the craniotomy to the hilar region using a 0.35 μl injection volume that was injected 2 mm deep (from the dural surface). After injection, the injection needle was retracted to a depth of 1.8 mm and was kept there for about 10 min before it was withdrawn completely. All experiments were conducted after a minimum of 3 weeks of recovery following the operation. For optogenetic stimulation, the viral construct AAV5-DIO-ChR2(H134R)-eYFP was used for the patch-clamp recording experiments in the lab of Dr. Lien in Taipei, and AAV1-DIO-ChR2(H134R)-mCherry was used for the behavioral experiments and *in vivo* recordings in the lab of Dr. Monyer in Heidelberg. Two viruses were used for Cre-dependent ChR2 transduction because experiments were carried out at two institutions where these virus tools were already established. For optogenetic inhibition, the viral construct AAV5-DIO-eNpHR3.0-eYFP was used. As control viruses we employed AAV1-DIO-eYFP and AAV5-DIO-eYFP. All viruses were obtained from Addgene (#37082, 26966, 27056, and 55639). Retrograde tracing was performed using the retrograde tracer cholera toxin subunit B tagged with Alexa Flour-555 (CTB-555; Invitrogen; Wan et al., 1982).

For *in vivo* unit recordings customized microdrives (Axona, MDR-16TSS1) with four individually movable tetrodes were used. Each tetrode was constructed by twisting four tungsten wires (12 μm; California Fine Wire) tightly together. An optical fiber (Doric lenses, 125-0.22_18mm_ZF1.25-FLT) was placed in the midst between the four tetrodes. Implantation coordinates were DV -1.7 mm for the optical fiber and DV -1.3 mm for tetrodes. For the behavioral experiments, all virus injections were into the left DG, and the optical fiber (Thorlabs, CFML22U-20) was implanted above the right DG (DV: -1.7 mm).

Slice electrophysiology

We used 52 mice for mapping the contralateral targets of DG SOM^+ cells. To prepare brain slices for patch-clamp recordings, coronal brain slices of 300 μm thickness containing the DG with a midline cut were prepared from SOM-Cre mice injected with a ChR2-virus using a vibratome (Dosaka, DTK-1000). The brains were rapidly isolated and sliced in ice-cold cutting saline containing the following

(in mM): 87 NaCl, 25 $NaHCO_3$, 1.25 NaH_2PO_4, 2.5 KCl, 10 glucose, 75 sucrose, 0.5 $CaCl_2$, and 7 $MgCl_2$. After sectioning, the slices were incubated in oxygenated (95% O_2/5% CO_2) cutting saline in a recovery chamber at 34°C for 30 min and stored at 23–25°C until ready for use. During the recordings, the slices were placed in a recording chamber and perfused with oxygenated artificial cerebrospinal fluid (ACSF) containing the following (in mM): 125 NaCl, 25 $NaHCO_3$, 1.25 NaH_2PO_4, 2.5 KCl, 25 glucose, 2 $CaCl_2$, and 1 $MgCl_2$. Neurons were visualized under an infrared differential interference contrast microscope (Olympus, BX51WI). The optical stimuli were captured using a GaP photodiode (Thorlabs, wavelength range, 150–550 nm; 1 ns rise time), and the signals of the photodiode were simultaneously recorded with the physiological signals. Whole-cell recordings were performed using a MultiClamp 700B amplifier (Molecular Devices). Recording pipettes (2–5 MΩ) were pulled from borosilicate glasses with a filament (Harvard Apparatus, outer diameter 1.5 mm; thickness, 0.32 mm). The recording pipettes were filled with an internal solution containing the following (in mM): 15 K-gluconate, 140 KCl, 0.1 EGTA, 2 $MgCl_2$, 4 Na_2ATP, 10 HEPES, and 0.4% biocytin (w/v) (310 mOsm/L). The broad-spectrum ionotropic glutamate receptor blocker kynurenic acid (2 mM) and the $GABA_A$ receptor antagonist gabazine (1 μM) were used to block glutamatergic and GABAergic transmission, respectively. Of the 281 patched neurons, 124 were classified as responsive, and of these 61 were recorded from the left hemisphere and the others from the right hemisphere. For all recordings, the pipette capacitance was fully compensated, and the series resistance was compensated to approximately 80% in the voltage-clamp configuration. Signals were low-pass filtered at 4 kHz and sampled at 10 kHz using Digidata 1440A (Molecular Devices). Pulse sequences were generated using pClamp 10.2 (Molecular Devices). All recordings were performed at 23–25°C.

Neuron-labeling and reconstruction

To identify the recorded cells in slice recordings, we filled the cells with the biocytin-containing internal solution for at least 30 min. The cells were subsequently fixed overnight in 4% paraformaldehyde (PFA). After fixation, the slices were permeabilized with 0.3% Triton X-100 and incubated with Alexa-594-conjugated avidin (1:400, Invitrogen) overnight at 4°C. The brain slices were mounted with Vectashield mounting medium (Vector Laboratories). Neurons labeled with Alexa-594-avidin were scanned using a two-photon microscope with a pulsed titanium sapphire laser (Coherent, Chameleon-Ultra II tuned to 800 nm) attached to a Leica DM6000 CFS equipped with a 20×/1.0 NA water immersion objective (Leica, HCX APO L). Morphological reconstructions were performed using Neuromantic 1.6.3 software (Myatt et al., 2012).

In vivo unit recordings

After full recovery from the surgery, the mice were deprived of food, and their body weights were maintained above 85% of their original weights. Mice (n = 13) on food restriction were encouraged to explore and forage in a 70 × 70 × 30 cm square box (exploration session), where small food pellets (TestDiet, 5 mg) were distributed automatically at 25 to 55 s intervals from a pellet feeder placed 100 cm above the center of the exploration box. After habituation to the environment was completed, two objects containing diluted vanilla essence (1:100, Dr. Oetker Butter-Vanille-Aroma) were placed in the recording box as the enriched environment would increase DG activity (Heale and Vanderwolf, 1994; Huckleberry et al., 2015; Kirschen et al., 2017). The objects were placed 20 cm away from the walls (4 candidate spots). The recording session started after the mice were fully habituated to the environment and the objects (approximately two weeks; Kirschen et al., 2017). A recording session comprised two 20 min exploration trials with 10 min rest in between (rest box; 20 × 20 × 30 cm). The objects were placed randomly in 2 of 4 candidate spots in the first exploration trial. For the second exploration trial, one object was displaced such that it was orthogonal to its original position. The placement was repeated the next day with a reversed light-on/-off assignment (Figure 2A, bottom), and the object location and stimulation were balanced throughout the recordings. Tetrodes were advanced by approximately 25 μm after two recording sessions.

The microdrive was connected to a LED-anchored headstage (Intan, RHD2132) that amplified and digitized the signals, and was further connected to an interface board (Intan, RHD USB interface board; analog bandwidth, 0.09–7603.77 Hz; sampling rate, 20 kHz) with a lightweight cable (Intan, RHD 6-ft ultra thin SPI cable). The signals from the interface board were sent to a computer where data were acquired and stored using the open-source software Ktan (https://github.com/kevin-allen/ktan) as described previously (Kornienko et al., 2018). Automatic clustering was first performed using KlustaKwik (https://sourceforge.net/projects/klustakwik/; Rossant et al., 2016), and cluster cutting was performed using Klusters (Lynn Hazan, Buzsáki lab). The position of animals was determined by tracking the LED signals using the open-source software Positrack (https://github.com/kevin-allen/positrack) sampled at 50 Hz. Randomized 10 Hz trigger signals for the photostimulation (~9.5 mW) were generated using the open-source software Laser_stimulation (https://github.com/kevin-allen/laser_stimulation). Digital on/off signals from the tracking and laser stimulation systems were transferred to the Intan USB interface board for synchronization with the physiological signals.

Criteria to determine responsive cells

To identify the directly targeted cells in the *ex vivo* recordings, we analyzed the average inhibitory postsynaptic currents (IPSCs). A cell was considered responsive when the peak amplitude of average IPSCs was greater than 3-fold the standard deviation (SD) of the baseline. In the *in vivo* recordings, we considered a cell responsive (excited or inhibited) when post optogenetic stimulation the number of spikes in two consecutive bins was greater than the mean ± 3-fold SD of the spike numbers in the baseline (20 ms before light stimuli) in the peristimulus histogram (1 ms bin size, 100 ms window size). The latency of the response was the time of the first bin when excitation or inhibition exceeded the threshold value.

Physiological features of neurons recorded *in vivo*

The burst index was calculated from the autocorrelogram of a single cell by dividing the spike number in the 3–5 ms bins by the average spike number in the 200–300 ms bins (Senzai and Buzsáki, 2017). The trough-to-peak latency was measured as the time from the most negative voltage of a spike to the highest voltage after that time point (Kornienko et al., 2018). The spatial information score was calculated as previously reported (Skaggs et al., 1993). The information score indicates the amount of spatial information (bits) encoded by a spike. The following formula was used:

$$Information\ \ score\ =\ \sum_{i=1}^{N} p_i \frac{\lambda_i}{\lambda} log_2 \frac{\lambda_i}{\lambda}$$

The space of the recording chamber is divided into nonoverlapping spatial bins where $i = 1, \ldots, N$ bin, p_i is the occupancy probability of the i^{th} bin, λ_i is the mean firing rate of the i^{th} bin, and λ is the overall mean firing rate of the cell.

Criteria to define spatial-selective cells

A cell was considered as spatial-selective if its information score was significantly higher than the information score obtained from the shuffled data (GoodSmith et al., 2017; $p < 0.05$). The shuffling procedure was repeated 1,000 times for each cell, and the the 95th percentile was selected as the cutoff for the information score obtained for the shuffled data. To exclude putative interneurons, only cells with a mean firing rate of < 10 Hz during light-off sessions were included in the analysis (GoodSmith et al., 2019).

Immunohistochemistry

Mice were perfused with 4% PFA (Carl Roth GmbH, Histofix) and the brain was post-fixed overnight. Endogenous mCherry signals were enhanced with polyclonal rabbit-anti-DsRed antibody (1:1000, Clontech Living Colors®, 632496) and Cy3-goat anti-rabbit antibody (1:1000, Jackson ImmunoResearch, 711-165-152). SOM and glutamate receptor subunit 2/3 (GluR2/3) expression were evaluated using rat monoclonal anti-SOM antibody (1:500, Millipore, MAB354) and rabbit polyclonal anti-GluR2/3 antibody (1:200, Millipore, AB1506), respectively. The slices were mounted with Mowiol (Mowiol 40-88, Sigma Aldrich, 324590-100G) and imaged using a confocal microscope (Zeiss, LSM 700).

Conditioned place preference test

The conditioned place preference (CPP) apparatus consisted of two chambers of the same size (20 × 20 × 27 cm), which were connected to a corridor (20 × 9 × 27 cm). The two chambers had a distinct pattern on their walls (“stripes” and “pattern”), which had a similar overall brightness. The entire apparatus was placed in a dimly lit room with prominent distal cues. On day 1 (pretest), the animals (eYFP: 17 mice, ChR2: 14 mice) received intraperitoneal saline (0.9% NaCl; 10 mL/kg) injection and were allowed to explore the CPP apparatus for 0.5 h. Allocation of the context (stripes, pattern), which would subsequently be paired with ethanol was performed in a counterbalanced manner. Mice that had pretest bias of over 25% more time in one chamber than the other during the pretest session were excluded. From days two to seven (except day five), each mouse was injected with saline in the morning immediately before entering the saline-paired chamber and injected with 2g/kg ethanol at a volume of 10ml/kg (20% ethanol in saline) in the afternoon immediately before entering the ethanol-paired chamber. The inverse regime, that is the ethanol session in the morning and the saline session in the afternoon, is not feasible, as it is likely that the effect of the ethanol administration in the morning session may not have worn off before the afternoon session. On day three and day six, the animals were habituated with a patch cable connected to the optical fiber in the morning sessions. On day eight (test), the animals received intraperitoneal saline and were allowed to freely explore the CPP apparatus for 0.5 h, while receiving 10 Hz blue light stimulations in the cDG. The CPP score was calculated as the time difference between the ethanol-paired and saline-paired chambers. During conditioning, we did not see a difference in locomotor activity between the ChR2 and eYFP groups (data not shown).

Object displacement (OD) and object recognition (OR) task

Three weeks after virus injection and optical fiber implantation, the animals (eYFP: 16 mice; NpHR: 17 mice) were carefully handled until they were fully habituated to human handling before performing the test (Hurst and West, 2010). The OD and OR experiments took 13 days in total. In spite of the difference in the apparatus between the OD and OR tasks, the experimental procedures were identical (Figures 4B and 4E): After an habituation trial (15 min) on the first day (Day 1), the mice were presented with the OD task (Day 2). The mice first explored the OD arena for 10 min during the sample session in which two identical objects of 6 cm diameter were placed 6 cm from the walls of the apparatus. After this trial the mice were placed to a resting box while the experimenter cleaned and set up the object configuration (OD: displace one object to a novel location; OR: replace one object with a novel object). After 5 min of delay, half of the mice received continuous 589 nm laser stimulations (~9.5 mW, OEM Laser Systems) during the 5 min test trial, while half of them received sham stimuli (laser-off). On the next day (Day 3), the mice that received laser stimuli previously received sham stimulation (laser-off), and vice versa for the other half of the mice. Six days (Day 9) after the laser manipulation during the test trials, mice repeated the OD task, with the difference that laser manipulation was delivered during the 10 min sample trial. Same procedure was applied for the OR task (starting from Day 5). The apparatus used in the OD task was a square arena (45 × 45 × 25 cm), and the one for the OR task was a circular arena (diameter 40 cm, height 40.5 cm). The video analysis

of exploratory behavior was performed at 0.5x playback speed, and the experimenter was blinded to the type of virus injection. Exploratory behavior was defined as the mouse being close to the object with the nose pointing toward, including sniffing or touching the object with the nose or forepaws. A discrimination index (DI) was calculated as follows:

$$Discrimination\ \ index(DI) = \frac{(T_{novel} - T_{familiar})}{(T_{novel} + T_{familiar})} \times 100\%$$

QUANTIFICATION AND STATISTICAL ANALYSIS

Data were analyzed using Clampfit 10.2 for *ex vivo* data, R 3.6, relectro (https://github.com/kevin-allen/relectro/) for *in vivo* data, DeepLabCut (Mathis et al., 2018) and Noldus for evaluating animal position in OD/OR and CPP experiments, respectively. The data in all graphs are presented as the mean +standard error of the mean (SEM) or mean + standard deviation (SD). The error bars in the bar graphs also denote SEMs or SDs. All statistical tests were two-sided with $\alpha = 0.05$. The medians for the between-group comparisons were tested using the Mann-Whitney U test and Kruskal-Wallis test with Dunn's tests, and Wilcoxon signed-rank tests for within-group comparisons. Multiple comparisons were analyzed using a *post-hoc* Tukey or Sidak test. GraphPad Prism 8 was used for the statistical analysis.